Simulation of electromagnetic ion cyclotron triggered emissions in the Earth's inner magnetosphere

Shoji, Masafumi; Omura, Yoshiharu

JOURNAL OF GEOPHYSICAL RESEARCH, VOL. 116, A05212, doi:10.1029/2010JA016351, 2011

Simulation of electromagnetic ion cyclotron triggered emissions in the Earth's inner magnetosphere

Masafumi Shoji[1] and Yoshiharu Omura[1]

Received 6 December 2010; revised 24 January 2011; accepted 17 February 2011; published 18 May 2011.

[1] In a recent observation by the Cluster spacecraft, emissions triggered by electromagnetic ion cyclotron (EMIC) waves were discovered in the inner magnetosphere. We perform hybrid simulations to reproduce the EMIC triggered emissions. We develop a self-consistent one-dimensional hybrid code with a cylindrical geometry of the background magnetic field. We assume a parabolic magnetic field to model the dipole magnetic field in the equatorial region of the inner magnetosphere. Triggering EMIC waves are driven by a left-handed polarized external current assumed at the magnetic equator in the simulation model. Cold proton, helium, and oxygen ions, which form branches of the dispersion relation of the EMIC waves, are uniformly distributed in the simulation space. Energetic protons with a loss cone distribution function are also assumed as resonant particles. We reproduce rising tone emissions in the simulation space, finding a good agreement with the nonlinear wave growth theory. In the energetic proton velocity distribution we find formation of a proton hole, which is assumed in the nonlinear wave growth theory. A substantial amount of the energetic protons are scattered into the loss cone, while some of the resonant protons are accelerated to higher pitch angles, forming a pancake velocity distribution.

Citation: Shoji, M., and Y. Omura (2011), Simulation of electromagnetic ion cyclotron triggered emissions in the Earth's inner magnetosphere, *J. Geophys. Res.*, *116*, A05212, doi:10.1029/2010JA016351.

1. Introduction

[2] ULF waves called Pc1–2 (0.1–5 Hz) pulsations consisting of L-mode electromagnetic ion cyclotron (EMIC) waves have been observed on the ground [*Troitskaya*, 1961; *Tepley*, 1961] and in the Earth's magnetosphere at various latitudes by many spacecraft (e.g., GEOS-2 [*Roux et al.*, 1982], AMPTE CCE [*Anderson et al.*, 1992a, 1992b], Viking [*Erlandson et al.*, 1990, 1996; *Mursula et al.*, 1997], Freja [*Mursula et al.*, 1994], Polar [*Mursula et al.*, 2001; *Arnoldy et al.*, 2005], and Cluster [*Engebretson et al.*, 2007]). A recent Cluster observation around the equatorial region of the inner magnetosphere discovered coherent ULF rising tone emissions [*Pickett et al.*, 2010] whose frequency characteristics are very similar to those of whistler mode VLF chorus emissions [*Santolik et al.*, 2003b; *Omura et al.*, 2008, 2009]. These ULF emissions arise from almost constant frequency waves lower than the proton cyclotron frequency ~3.7 Hz. The observation result indicates that these rising tone emissions always need the Pc1 (EMIC) pulsations as triggering waves. They call these chorus-like ULF emissions EMIC triggered emissions [*Pickett et al.*, 2010; *Omura et al.*, 2010].

[3] *Omura et al.* [2010] have developed a nonlinear wave growth theory explaining the EMIC triggered emissions. They found a good agreement between theory and observations in the frequency sweep rate of the rising tone emissions. The saturation mechanism of the wave growth, however, has not been explained by the theory yet. To understand the nonlinear processes including the saturation and associated pitch angle scattering of energetic protons, we need to analyze the time evolution of the interaction between the EMIC triggered emissions and the energetic protons quantitatively.

[4] In the present study, we reproduce the generation process of the EMIC triggered emissions by a self-consistent hybrid code with a parabolic magnetic field. We perform a hybrid simulation with realistic parameters around the magnetic equator at $L \sim 4.3$, and compare the results with the observations and theory. We first describe the simulation model and parameters in section 2. The simulation results are shown and discussed in section 3. These results show a good agreement with the nonlinear growth theory [*Omura et al.*, 2010] and a significant proton precipitation induced by the triggered emissions. Section 4 summarizes the simulation results.

2. Simulation Model and Parameters

[5] We have developed a self-consistent one-dimensional (1-D) hybrid model along the background magnetic field in the x direction. The algorithm of the hybrid code is described by *Shoji et al.* [2009]. In the hybrid simulation the

[1]Research Institute for Sustainable Humanosphere, Kyoto University, Kyoto, Japan.

0148-0227/11/2010JA016351

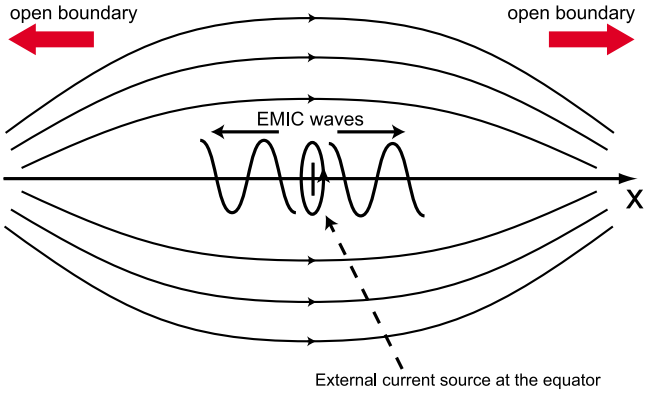

Figure 1. Schematic illustration of the hybrid simulation model.

displacement current and the electron inertia are neglected, and these assumptions are consistent with the nonlinear wave growth theory [*Omura et al.*, 2010]. A schematic illustration of the simulation model is shown in Figure 1. While the field equations are solved as the 1-D system taken along the x axis, the background magnetic field has a cylindrical geometry around the x axis, and ions are assumed to gyrate around the magnetic field with finite cyclotron radii. The magnetic equator is assumed at the center of the model ($x = 0$), and the x component of the background magnetic field is defined by a parabolic function as an approximation of the dipole magnetic field of the Earth:

$$B_{0x}(x) = B_{0eq}\left(1 + ax^2\right), \tag{1}$$

where B_{0eq} is the value at the equator, $a = 4.5/(LR_E)$, $L = 4.3$ and the Earth's radius R_E = 6,387 km. To satisfy the condition $\nabla \cdot \mathbf{B} = 0$, we assume the radial component of the ambient magnetic field as

$$B_{0r} = -\frac{r_{Li}}{2}\frac{\partial B_{0x}}{\partial x}, \tag{2}$$

where $r_{Li} = v_\perp/\Omega_{ci}$ is the Larmor radius of ions, and Ω_{ci} is the local cyclotron frequency of ions of species i. The same cylindrical geometry is assumed in recent simulation studies of whistler mode chorus emissions [*Katoh and Omura*, 2007; *Omura et al.*, 2008; *Hikishima et al.*, 2009a, 2009b, 2010].

[6] The triggering wave is excited at the equator by an external current source. When a linearly polarized current source with a fixed frequency is used, both R-mode and L-mode EMIC waves are excited as shown in Figure 2a. The R-mode wave has a smaller wavelength than that of the L-mode wave, and thus we can find these waves separately in Figure 2a. Since the R-mode wave has a larger group velocity than that of the L-mode EMIC wave, the simulation space is filled with the R-mode wave, which induces thermal fluctuations of energetic particles, disturbing the subsequent L-mode wave. To obtain a coherent monochromatic L-mode EMIC wave without the R-mode wave, we need to use a left-handed polarized current source. The current source is modeled by five grid points around the equatorial region and we specify both frequency and wave number of the triggering waves. To suppress an initial response of the magnetic field to the source current, we increase the magnitude of the current gradually in time. As shown in Figure 2b, monochromatic L-mode EMIC waves propagate away from the source current without foregoing R-mode waves.

[7] An open boundary condition is assumed for the x direction. Dumping layers are attached at both ends of the physical region. The transverse wave magnetic fields are dumped as $B_{dump}(x) = r(x)B(x)$ at each time step, where $r(x)$ is the masking function. The masking function $r(x)$ is defined as

$$r(x) = \begin{cases} 1 & (|x| \le X/2) \\ 1 - r_D\dfrac{(|x| - X/2)^2}{L_D^2} & (|x| > X/2), \end{cases} \tag{3}$$

where X is the size of the simulation space, L_D is the length of the damping region in each direction and $r_D = 0.0129$ is a coefficient for the best dumping effect given by the experimental equation [*Umeda et al.*, 2001]. At each boundary, 1,024 grids are used as the dumping region.

[8] The parameters of ions in the hybrid simulation are shown in Table 1, where c is the speed of light in vacuum, n_e = 178/cc is the density of the electron fluid, e is the elementary charge, m_H is the mass of the proton, q/m is the charge-to-mass ratio of ions, and N_p/cell is the average number of superparticles in a cell. Four kinds of ion species are assumed. Of the four, H^+, He^+ and O^+ are assumed as cold plasma components without thermal distributions. Their densities are assumed so that the wave dispersion relation gives the observed cutoff frequency. Energetic H^+

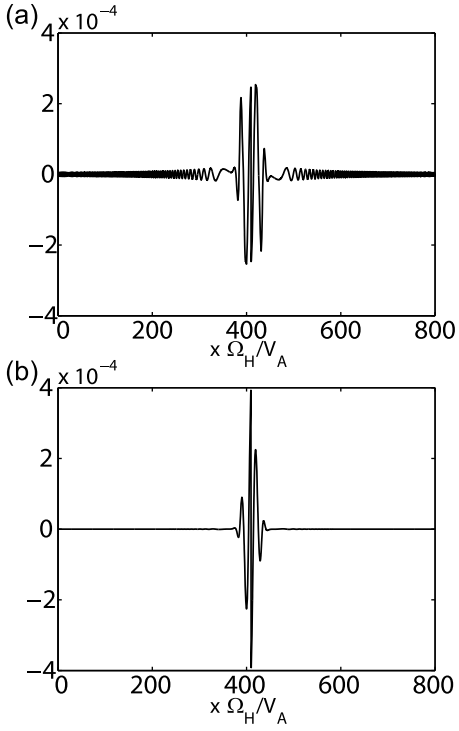

Figure 2. Waveforms of the test simulations with (a) a linear polarized current source and (b) a left-handed polarized current source.

Table 1. Parameters of Ion Species

Ion Species	$V_{th\parallel}/c$	$V_{th\perp}/c$	n_i/n_e	$q/m/(e/m_H)$	N_p/cell
H^+	0	0	0.7695	1.0	256
He^+	0	0	0.0950	1/4	256
O^+	0	0	0.0950	1/16	256
Energetic H^+	0.002	0.00267	0.0405	1.0	16,384

ions with temperature anisotropy are introduced as resonant particles with EMIC waves, forming a loss cone distribution function expressed by

$$f(v_\parallel, v_\perp) = \frac{n_h}{(2\pi)^{3/2} V_{th\parallel} V_{th\perp}^2} \exp\left(-\frac{v_\parallel^2}{2V_{th\parallel}}\right) g(v_\perp), \quad (4)$$

where n_h, $V_{th\parallel}$, and $V_{th\perp}$ are the density, thermal velocities in the parallel and perpendicular directions of energetic protons, respectively. The function $g(v_\perp)$ is defined as

$$g(v_\perp) = \frac{1}{1-\beta}\left\{\exp\left(-\frac{v_\perp^2}{2V_{th\perp}^2}\right) - \exp\left(-\frac{v_\perp^2}{2\beta V_{th\perp}^2}\right)\right\}, \quad (5)$$

where $\beta = 0.1$. The quiet start [*Birdsall and Langdon*, 1985] is used to reduce the initial thermal fluctuations. The quiet start requires pairs of particles with the same positions and parallel velocities. The particles of each pair have opposite perpendicular velocities with the same magnitude forming no current in the transverse plane initially. The energetic protons are initialized to form a spatial distribution that is stable in time with adiabatic motion in the parabolic magnetic field.

[9] According to the observational results [*Omura et al.*, 2010], the cyclotron and the plasma frequency of protons are assumed as 3.7 Hz and 353.4 Hz, respectively, at the magnetic equator. Thus the amplitude of the ambient magnetic field is $B_{0eq} = 243$ nT, and the Alfven velocity is 443 km/s at the equator. The number of grids of the physical region is $n_x = 4{,}096$ with the grid spacing $\Delta x = 0.1 V_A/\Omega_H (= 1.9$ km), and the time step is $\Delta t = 0.004/\Omega_H (= 1.72 \times 10^{-4}$ s), where V_A and Ω_H are the Alfven velocity and the cyclotron frequency of the cold protons at the equator. The frequency and the wave number of the triggering waves are taken from the observation as $(\omega_w, k_w) = (0.409\Omega_H, 0.27\Omega_H/V_A)$, which is $(f_w, k_w/(2\pi)) = (1.5$ Hz, 2.2×10^{-3}/km) in the real unit system. The wave amplitude of the triggering wave is $B_w = 0.5$ nT. The theoretical amplitude threshold derived by *Omura et al.* [2010] is 0.41 nT. Thus, the wave amplitude is large enough to drive the nonlinear growth of the EMIC triggered emissions. In this model, we do not calculate the parallel motion of cold ions supporting the propagation of waves. We also note that the parallel components of the electric field and the current density are not solved, because we only have purely transverse waves propagating along the magnetic field line in the present simulation.

[10] The linear dispersion relation of the L-mode EMIC wave [*Stix*, 1992] in the cold plasma approximation is given by

$$c^2k^2 = \omega\left(\sum_s \frac{\omega_{ps}^2}{\Omega_s - \omega} - \frac{\omega_{pe}^2}{\Omega_e}\right), \quad (6)$$

where c, ω_{ps}, and Ω_s are the speed of light, plasma and cyclotron frequencies of ion species s, respectively. The plasma and cyclotron frequencies of electrons are ω_{pe} and Ω_e, respectively. Figure 3 shows the linear dispersion relation of the EMIC wave with the parameters used in the hybrid simulation. In this model, we assume three different species of cold ions. The top, middle, and bottom branches in the ω-k diagram correspond to EMIC modes bounded by the cyclotron frequencies of proton, helium and oxygen ions, respectively. The dashed lines show the frequency and wave number of the triggering waves. In the observations [*Pickett et al.*, 2010; *Omura et al.*, 2010], the frequency and the wave number of the EMIC triggered emissions varied in about 40 s in the ranges of the proton branch shown by the arrows (from dashed lines to dotted lines).

3. Hybrid Simulations: Results and Discussions

[11] A Fourier transform along the x direction is applied to the transverse EMIC wave magnetic field to obtain $\mathbf{B}_\perp(k, t)$ at each time step. Considering the polarization of the EMIC waves, we separate the magnetic field into forward propagating waves $\mathbf{B}_f(k, t)$ and backward propagating waves $\mathbf{B}_b(k, t)$ which have positive and negative wave numbers, respectively. Then we apply the inverse Fourier transform for the separated modes and we obtain the EMIC waves propagating with positive or negative wave numbers. The wave amplitudes of the forward and the backward waves are plotted as functions of x and t in Figure 4. From $t \sim 15$s, both forward and backward triggered waves start to be generated in the regions where there is no triggering wave in the same propagation direction.

[12] The distance between the generation region of the triggered waves and the equatorial region becomes larger as the emission proceeds. The forward and backward propagating triggering waves interact with the backward and forward moving energetic protons, respectively. The energetic protons interacting with the triggering waves are phase organized in the transverse wave plane around the equatorial region. These protons are released at the equator and move into the region where there is no triggering wave. They form the transverse currents and generate seeds of the triggered

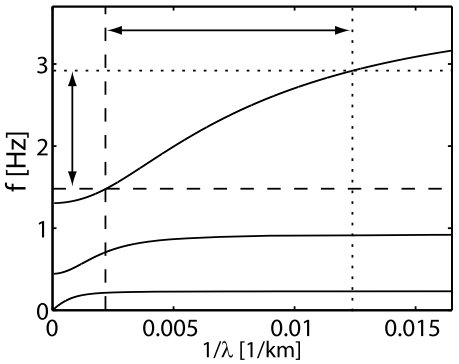

Figure 3. Dispersion relation of the L-mode EMIC waves with frequency $f = \omega/(2\pi)$ and wave number $1/\lambda = k/(2\pi)$. The dashed lines show the initial frequency and the wave number of the triggering wave. The dotted lines indicate the ending frequency and wave number of the triggered wave.

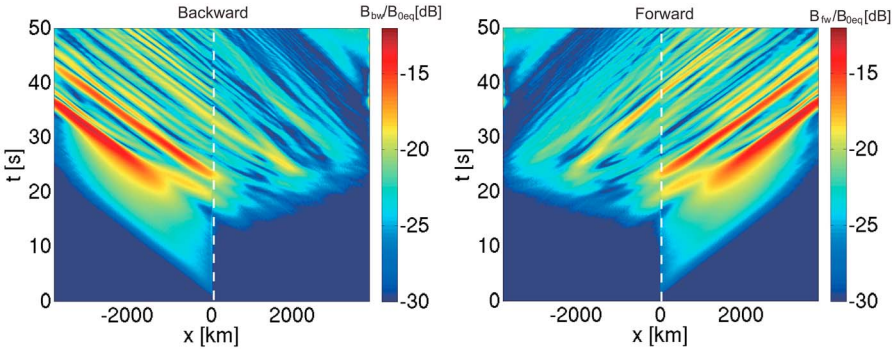

Figure 4. Spatial and temporal evolution of the wave amplitudes of the backward and forward propagating EMIC waves.

emissions propagating in the opposite direction. The phase-organized protons move away from the equator and thus the regions where the triggered emissions are generated move with these particles.

[13] The frequency sweep rate of the triggered wave at the equator is theoretically given by [*Omura et al.*, 2010]

$$\frac{\partial \omega}{\partial t} = \frac{0.4 s_0}{s_1} \omega \Omega_{w0}, \tag{7}$$

where $s_0 = V_{th\perp}/V_p$, $s_1 = (1 - V_R/V_g)^2$, $V_p = \omega/k$ is the phase velocity, $V_R = (\omega - \Omega_H)/k$ is the resonance velocity, $V_g = \partial\omega/\partial k$ is the group velocity, and $\Omega_{w0} = eB_{w0}/m_H$ is the normalized amplitude of the triggered wave at the equator. The time evolution of B_{w0} at the equator is shown in Figure 5a. The triggered wave saturates around $t \sim 24$ s. We find a good agreement of the saturated amplitudes between the simulation and the observation results shown in Figure 7 of *Omura et al.* [2010]. We also show the frequency of the triggered wave as shown in Figure 5b. The frequency is calculated by integrating (7). The frequency starts to increase significantly when the wave amplitude start to grow. Even after the saturation, the frequency still increases.

[14] We apply a Fourier transform in a limited time window for both forward and backward propagating waves at the equatorial region. Sliding the window from the initial time to the end of the simulation period, we obtain the time

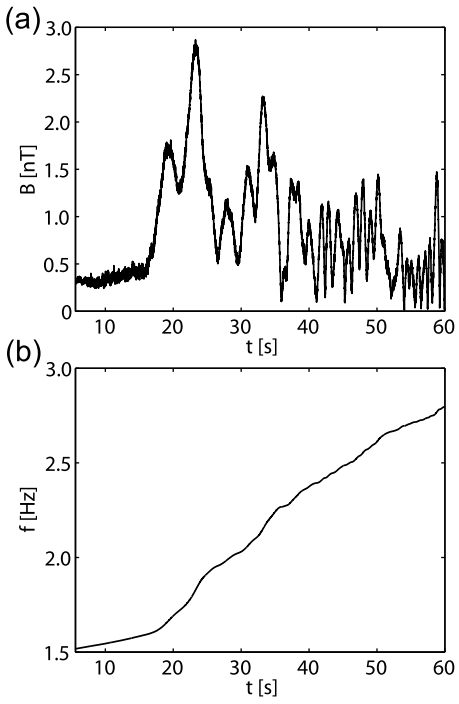

Figure 5. Time evolution of (a) the wave amplitude and (b) the theoretical frequency of the triggered wave at the equator.

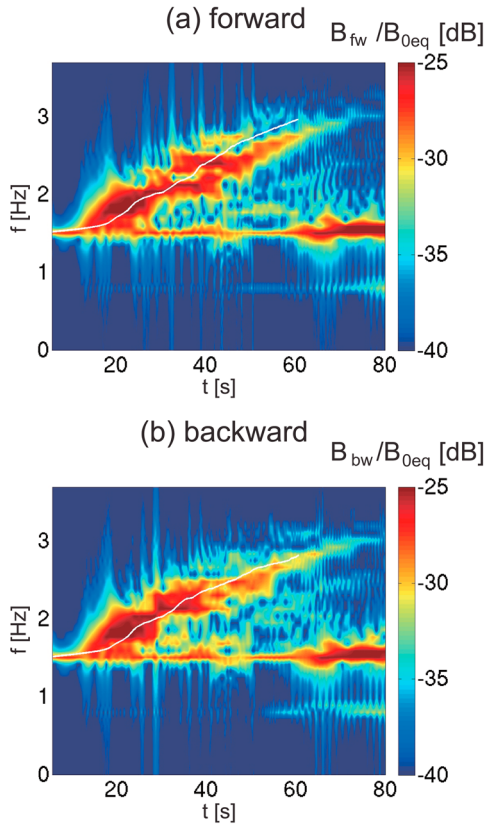

Figure 6. Dynamic spectra of the magnetic fields of (a) forward propagating waves and (b) backward propagating waves. The white lines show the theoretical frequency of the triggered waves.

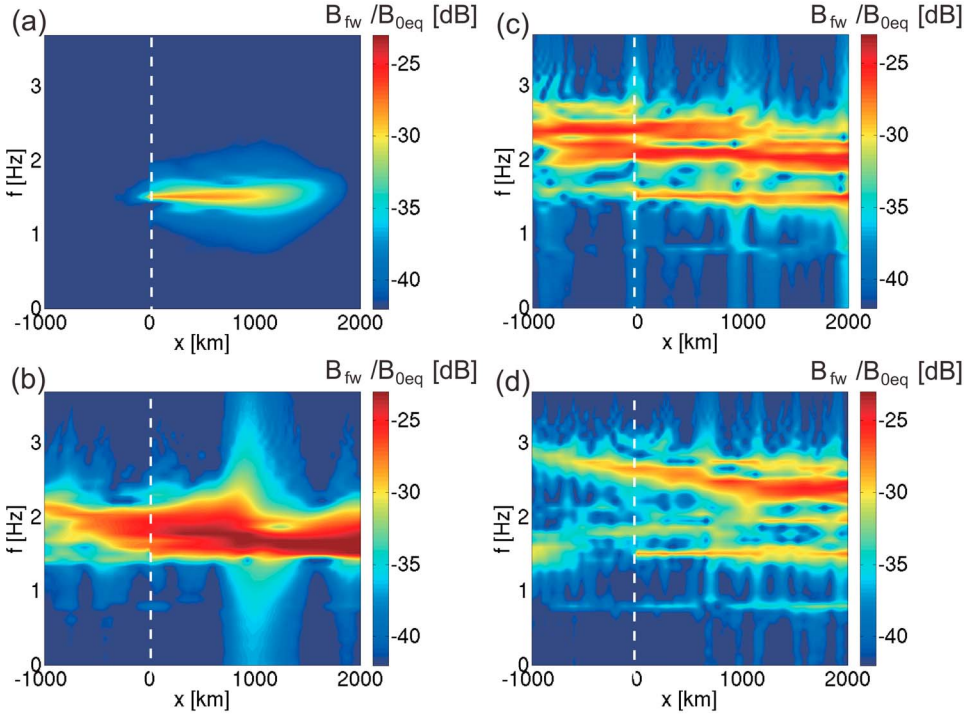

Figure 7. Spatial profiles of the wave spectra of the magnetic field at (a) $t = 5.6$ s, (b) $t = 22.1$ s, (c) $t = 38.8$ s, and (d) $t = 55.3$ s.

evolution of the wave spectra. The size of the window is taken as $t \sim 11.2$ s for a sufficient resolution in the frequency domain. Figures 6a and 6b show dynamic spectra of the forward and backward propagating waves around the equatorial region obtained by this method, respectively. In the case that we do not inject the triggering waves, although the result is not shown in this paper, there occurs no electromagnetic emission. On the other hand, as shown in Figures 6a and 6b, the EMIC triggered emissions are successfully reproduced both in the forward and backward propagating waves. This means that we need finite amplitude triggering waves to induce the EMIC triggered emissions. The duration of the rising tone emissions from 1.5 Hz to 3.0 Hz is 45 s in this case, showing a good agreement with the observation [*Pickett et al.*, 2010] and the theory [*Omura et al.*, 2010]. The frequency predicted by the theory is shown by the white line in Figures 6a and 6b. We find a good agreement with the theory in the initial phase of the triggered emissions. Because this theory does not include the saturation mechanism, the theoretical frequency becomes different from that of the simulation result after ~40 s.

[15] Spatial profiles of wave frequency spectra of the forward propagating waves are plotted at different times in Figure 7. A spectrum at time t is calculated in a time range [$t - 5.6$ s $t + 5.6$ s] which is the same as the time window used in Figure 6. In Figure 7a ($t = 5.6$ s) we only find the spectrum of the triggering wave. Around $t = 22.1$ s, shown in Figure 7b, a triggered emission emerges in the region before reaching the equator, where there is no triggering wave. This suggests that the emission is not generated directly by the triggering wave. However the resonant current is formed by energetic protons that have been phase organized by the triggering wave and it induces the emission. As shown in Figures 7c ($t = 38.8$ s) and 7d ($t = 55.3$ s), we can find that the triggered emissions are generated progressively at different frequencies before reaching the equator, and that they grow in amplitude as they propagates away from the equator. The critical distance h_c, at which the temporal and spatial derivatives in the inhomogeneity ratio [*Omura et al.*, 2010] become equal, is estimated as $h_c \simeq 320$ km. In the regions beyond the critical distance ($|x| > h_c$), the triggered waves undergo convective growth driven by the gradient of the magnetic field.

[16] Figure 8 shows the velocity distribution functions of energetic protons around the equatorial region at different times. The values of the velocity distribution functions are normalized by the maximum value of the initial velocity distribution function f_{0M}. We show these panels at equal time intervals of 26.4 s. The white solid lines indicate the resonance velocities V_R of the forward ($k > 0$) and backward ($k < 0$) propagating triggered waves. We also show the resonance velocities of the forward and backward triggering waves (= ±970 km/s) by white dashed lines. The initial distribution function is shown in Figure 8a. As the EMIC triggered emissions evolve in time, the resonant velocities become smaller in magnitude because of the increasing frequencies and wave numbers. Thus the energetic protons with smaller parallel velocities are strongly scattered as shown in Figures 8b–8d. At $t = 26.4$ s (shown in Figure 8b) the triggered waves saturate, we can find proton holes around the resonance velocities of the triggered wave. The trapping velocity of the triggered waves $V_{tr} = \sqrt{V_{th\perp}\Omega_w/k}$ approaches to ~80 km/s in Figure 8b. Energetic protons satisfying $V_R - V_{tr} < v_{\|} < V_R + V_{tr}$ are strongly scattered in their pitch angles. As we find in Figure 8c, the proton holes are gradually filled out by the scattered resonant protons.

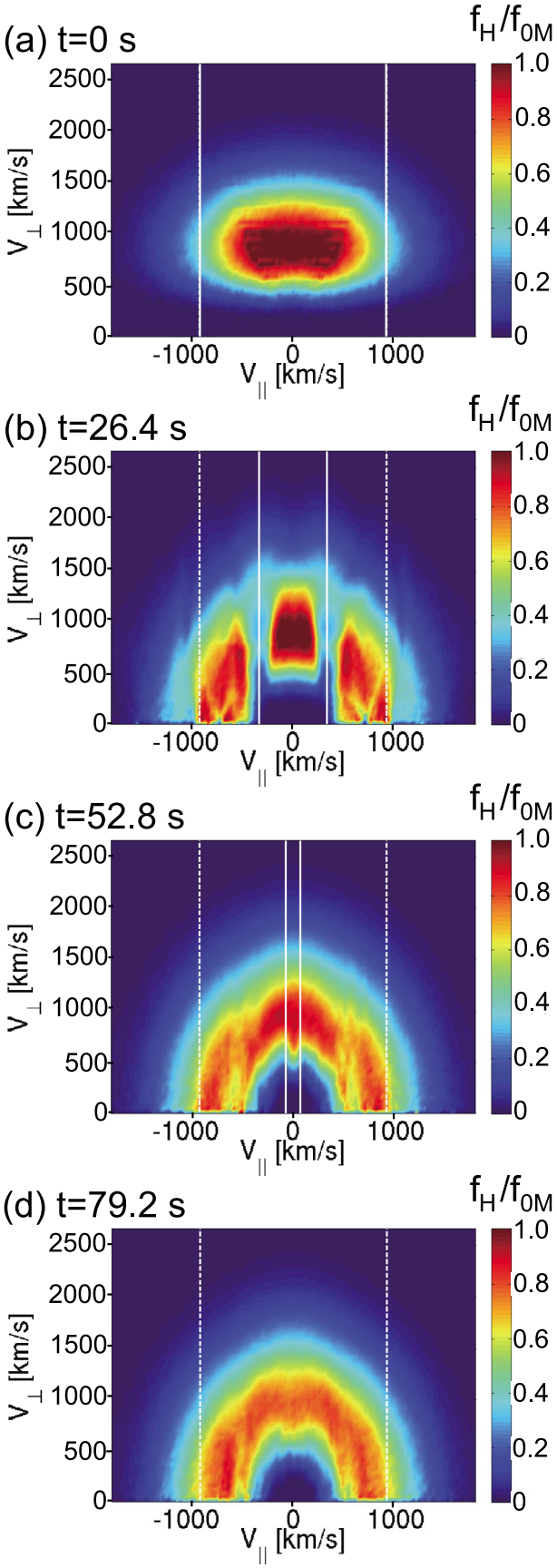

The frequencies of the triggered waves still increase and thus the core part of the distribution function of the energetic protons is diffused. Finally, as shown in Figure 8d after the triggered waves saturate and disappear, the distribution function becomes stable. At this time, the whole core of the initial distribution disappears. A substantial number of the energetic protons in a wide range of energy are scattered through the generation process of the triggered emissions. Thus the distribution of the energetic protons shows a very different distribution from the initial one, indicating strong pitch angle scattering by the triggered emissions over one cycle of the nonlinear triggering process.

[17] To understand the time evolution of the proton holes, we show fine time evolution of the distribution function during 17.6 s $\leq t \leq$ 35.2 s in Figure 9. Figure 9a shows the distribution function around the time when the triggered emission starts. At this time, the pitch angles of the energetic protons around the resonance velocities of the forward and backward propagating triggering waves are scattered. We continuously inject the triggering waves at the equator and the particles around the resonance velocities interact with the triggering waves. We also find significant depletion of energetic protons due to the proton holes at the resonance velocities in Figures 9b–9d. Through the inward motion of the proton holes, the core part of the velocity distribution erodes gradually in time, resulting in a pancake distribution near a pitch angle $\alpha = 90°$. As shown in Figures 9b–9e, the proton holes become smaller, when the amplitudes of the triggered waves decrease after the saturation around $t = 24$ s.

[18] Comparing Figures 8a and 8d, we find that the majority of energetic protons are scattered in their pitch angles. However, some of energetic protons are accelerated toward higher pitch angles. We define the difference of the velocity distributions as $\Delta f_H = f_H|_{t=79.2s} - f_H|_{t=0s}$ and plot it in Figure 10. Figure 10a shows the distribution of the accelerated particles which have $V_\perp >$ 1,600 km/s. The negative value in Figure 10b indicates the particle loss. Most of the lost particles are strongly scattered to lower pitch angles losing the energy while some of them are accelerated to higher pitch angles.

[19] From Figure 10a, we can find a clear increase of energetic protons around pitch angles ~90°. We integrate the increased density of the energetic protons which have $V_\perp >$ 1,600 km/s. During the generation process of the triggered emissions, nearly 2.4% of energetic protons in the equatorial region are accelerated. The acceleration is due to phase trapping of resonant protons guided from the upstream regions toward the equator along the resonance velocity, which decreases to the lower value in magnitude. Because of the energy transfer from the waves to the accelerated protons, the nonlinear wave growth near the equator is saturated, and triggered waves are subsequently damped.

Figure 8. Velocity distribution functions $f_H(v_{||}, v_\perp)$ of energetic protons at (a) $t = 0$ s, (b) $t = 26.4$ s, (c) $t = 52.8$ s, and (d) $t = 79.2$ s normalized by the maximum value of the initial velocity distribution function f_{0M}. The white dashed lines show the resonance velocities of forward and backward triggering waves. The white solid lines show those of forward and backward triggered waves.

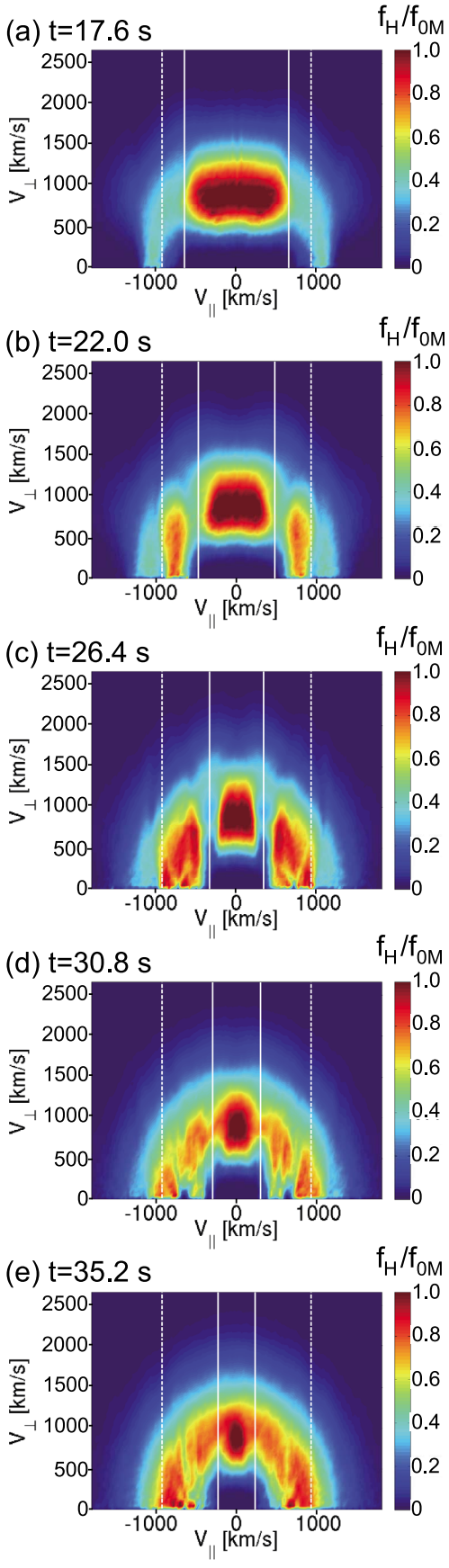

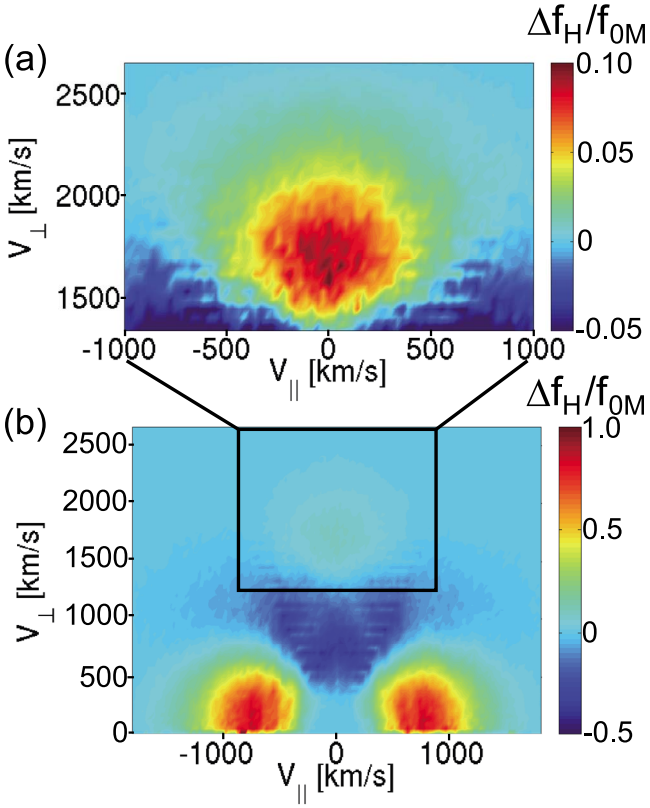

Figure 10. Difference of the velocity distribution functions of energetic protons, $\Delta f_H = f_H|_{t=79.2s} - f_H|_{t=0s}$, in regions where (a) 1,600 km/s < $V_\perp$ < 2,600 km/s and $|V_\parallel|$ < 1,000 km/s and (b) 0 km/s < $V_\perp$ < 2,600 km/s and $|V_\parallel|$ < 1,600 km/s. The value of Δf_H is normalized by the maximum value of the initial velocity distribution function f_{0M}.

[20] A large number of particles are scattered by the triggered emissions and some of them fall into the loss cone as shown in Figure 10b. The loss cone angle at the equator α_l [*Baumjohann and Treumann*, 1997] is given by

$$\sin^2 \alpha_l = \frac{1}{\sqrt{4L^6 - 3L^5}}. \quad (8)$$

All of the protons with pitch angles $\alpha < \alpha_l$ precipitate into the atmosphere. Assuming $L = 4.3$, we have $\alpha_l = 4.8°$, and we can estimate the amount of the precipitating protons from Figure 10b. We integrate the density difference of the energetic protons over the range of pitch angle $\alpha < \alpha_l$ in the velocity space. Through the EMIC triggered emission, 6.5% of the energetic protons precipitate into the atmosphere. The averaged proton energy at t = 79.2 s in the loss cone is 4.54 keV. Precipitation of these energetic particles can cause

Figure 9. Velocity distribution functions $f_H(v_\parallel, v_\perp)$ of energetic protons at (a) t = 17.6 s, (b) t = 22.0 s, (c) t = 26.4 s, (d) t = 30.8 s, and (e) t = 35.2 s normalized by the maximum value of the initial velocity distribution function f_{0M}. The white dashed lines show the resonance velocities of forward and backward triggering waves. The white solid lines show those of forward and backward triggered waves.

the proton aurora around the polar region [*Montbriand*, 1971; *Fukunishi*, 1975; *Spasojevic et al.*, 2004].

[21] *Pickett et al.* [2010] reported that more than two triggered emissions took place in a few minutes. As demonstrated in the present simulation, however, the free energy of energetic protons is completely consumed by a single emission process of an EMIC triggered emission. We only introduce the energetic protons initially and thus we obtain only one pair of triggered emissions in the simulation. The observed multiple triggered emissions require continuous injection of fresh energetic protons. Continuous generation of the triggering EMIC waves, which can be excited by the cyclotron instability driven by the temperature anisotropy of protons, is also needed.

4. Conclusions

[22] 1. We have developed a 1-D hybrid code with a cylindrical magnetic field model to analyze the nonlinear wave growth of EMIC triggered emissions in dipole geometry, reproducing the rising tone emissions from injected EMIC triggering waves around the equatorial region with realistic parameters. The duration and the frequency sweep rate of the triggered emissions show a good agreement with observations and nonlinear wave growth theory.

[23] 2. The proton velocity distribution is strongly modulated by formation of large proton holes due to the triggered emissions. The rising tone emissions drive the proton holes to a lower parallel velocity because of the decreasing resonance velocities.

[24] 3. A substantial amount of energetic protons as large as 6.5% of the trapped protons are scattered into the loss cone in 45 s during which the triggered emissions are generated inside the plasmapause. These particles move away from the equator along the ambient magnetic field, and precipitate into the atmosphere, resulting in the proton aurora in the polar regions.

[25] **Acknowledgments.** Computation in the present study was performed with the KDK system of the Research Institute for Sustainable Humanosphere and the Academic Center for Computing and Media Studies at Kyoto University as a collaborative research project. The present study was supported in part by Grant-in-Aid for Research Fellows from the Japan Society for the Promotion of Science and Grant-in-Aid 20340135 of the Ministry of Education, Science, Sports and Culture of Japan.

[26] Robert Lysak thanks Mark Engebretson and another reviewer for their assistance in evaluating this paper.

References

Anderson, B. J., R. E. Erlandson, and L. J. Zanetti (1992a), A statistical study of Pc 1–2 magnetic pulsations in the equatorial magnetosphere: 1. Equatorial occurrence distributions, *J. Geophys. Res.*, *97*, 3075.

Anderson, B. J., R. E. Erlandson, and L. J. Zanetti (1992b), A statistical study of Pc 1–2 magnetic pulsations in the equatorial magnetosphere: 2. Wave properties, *J. Geophys. Res.*, *97*, 3089.

Arnoldy, R. L., et al. (2005), Pc 1 waves and associated unstable distributions of magnetospheric protons observed during a solar wind pressure pulse, *J. Geophys. Res.*, *110*, A07229, doi:10.1029/2005JA011041.

Baumjohann, W., and R. A. Treumann (1997), *Basic Space Plasma Physics*, Imperial Coll. Press, London.

Birdsall, C. K., and A. B. Langdon (1985), *Plasma Physics Via Computer Simulation*, McGraw-Hill, New York.

Engebretson, M. J., et al. (2007), Cluster observations of Pc 1–2 waves and associated ion distributions during the October and November 2003 magnetic storms, *Planet. Space Sci.*, *55*, 829.

Erlandson, R. E., L. J. Zanetti, T. A. Potemra, L. P. Block, and G. Holmgren (1990), Viking magnetic and electric field observations of Pc 1 waves at high latitudes, *J. Geophys. Res.*, *95*, 5941.

Erlandson, R. E., K. Mursula, and T. Bosinger (1996), Simultaneous ground-satellite observations of structured Pc 1 pulsations, *J. Geophys. Res.*, *101*, 27,149.

Fukunishi, H. (1975), Dynamic relationship between proton and electron auroral substorms, *J. Geophys. Res.*, *80*, 553.

Hikishima, M., S. Yagitani, Y. Omura, and I. Nagano (2009a), Full particle simulation of whistler mode rising chorus emissions in the magnetosphere, *J. Geophys. Res.*, *114*, A01203, doi:10.1029/2008JA013625.

Hikishima, M., S. Yagitani, Y. Omura, and I. Nagano (2009b), Coherent nonlinear scattering of energetic electrons in the process of whistler mode chorus generation, *J. Geophys. Res.*, *114*, A10205, doi:10.1029/2009JA014371.

Hikishima, M., Y. Omura, and D. Summers (2010), Microburst precipitation of energetic electrons associated with chorus wave generation, *Geophys. Res. Lett.*, *37*, L07103, doi:10.1029/2010GL042678.

Katoh, Y., and Y. Omura (2007), Computer simulation of chorus wave generation in the Earth's inner magnetosphere, *Geophys. Res. Lett.*, *34*, L03102, doi:10.1029/2006GL028594.

Montbriand, L. E. (1971), The proton aurora and auroral substorm, in *The Radiating Atmosphere*, edited by B. M. McCormac, pp. 366–373, D. Reidel, Dordrecht, Netherlands.

Mursula, K., L. G. Blomberg, P. A. Lindqvist, G. T. Marklund, T. Braysy, R. Rasinkangas, and P. Tanskanen (1994), Dispersive Pc1 bursts observed by Freja, *Geophys. Res. Lett.*, *21*, 1851.

Mursula, K., R. Rasinkangas, and T. Bosinger (1997), Nonbouncing Pc 1 wave bursts, *J. Geophys. Res.*, *102*, 17,611.

Mursula, K., T. Braysy, K. Niskala, and C. T. Russell (2001), Pc1 pearls revisited: Structured electromagnetic ion cyclotron waves on Polar satellite and on the ground, *J. Geophys. Res.*, *106*, 29,543.

Omura, Y., Y. Katoh, and D. Summers (2008), Theory and simulation of the generation of whistler-mode chorus, *J. Geophys. Res.*, *113*, A04223, doi:10.1029/2007JA012622.

Omura, Y., M. Hikishima, Y. Katoh, D. Summers, and S. Yagitani (2009), Nonlinear mechanisms of lower-band and upper-band VLF chorus emissions in the magnetosphere, *J. Geophys. Res.*, *114*, A07217, doi:10.1029/2009JA014206.

Omura, Y., J. Pickett, B. Grison, O. Santolik, I. Dandouras, M. Engebretson, P. M. E. Decreau, and A. Masson (2010), Theory and observation of electromagnetic ion cyclotron chorus emissions in the magnetosphere, *J. Geophys. Res.*, *115*, A07234, doi:10.1029/2010JA015300.

Pickett, J. S., B. Grison, Y. Omura, M. J. Engebretson, I. Dandouras, A. Masson, M. L. Adrian, O. Santolik, P. M. E. Decreau, N. Cornilleau-Wehrlin, and D. Constantinescu (2010), Cluster observations of EMIC triggered emissions in association with Pc1 waves near Earth's plasmapause, *Geophys. Res. Lett.*, *37*, L09104, doi:10.1029/2010GL042648.

Roux, A., S. Perraut, J. Rauch, C. de Villedary, G. Kremser, A. Korth, and D. Young (1982), Wave-particle interactions near Ω_{He} observed on board GEOS 1 and 2: 2. Generation of ion cyclotron waves and heating of He+ ions, *J. Geophys. Res.*,*87*, 8174.

Santolik, O., D. A. Gurnett, J. S. Pickett, M. Parrot, and N. Cornilleau-Wehrlin (2003b), Spatio-temporal structure of storm-time chorus, *J. Geophys. Res.*, *108*(A7), 1278, doi:10.1029/2002JA009791.

Shoji, M., Y. Omura, B. T. Tsurutani, O. P. Verkhoglyadova, and B. Lembege (2009), Mirror instability and L-mode electromagnetic ion cyclotron instability: Competition in the Earth's magnetosheath, *J. Geophys. Res.*, *114*, A10203, doi:10.1029/2008JA014038.

Spasojevic, M., H. U. Frey, M. F. Thomsen, S. A. Fuselier, S. P. Gary, B. R. Sandel, and U. S. Inan (2004), The link between a detached subauroral proton arc and a plasmaspheric plume, *Geophys. Res. Lett.*, *31*, L04803, doi:10.1029/2003GL018389.

Stix, T. H. (1992), *Waves in Plasmas*, Am. Inst. of Phys., New York.

Tepley, L. R. (1961), Observations of hydromagnetic emissions, *J. Geophys. Res.*, *66*, 1651.

Troitskaya, V. A. (1961), Pulsations of the Earth's electromagnetic field with periods of 1 to 1.5 seconds and their connection with phenomena in the high atmosphere, *J. Geophys. Res.*, *66*, 5.

Umeda, T., Y. Omura, and H. Matsumoto (2001), An improved masking method for absorbing boundaries in electromagnetic particle simulations, *Comput. Phys. Commun.*, *137*, 286.

Y. Omura and M. Shoji, Research Institute for Sustainable Humanosphere, Kyoto University, Gokasho, Uji, Kyoto 611-0011, Japan. (omura@rish.kyoto-u.ac.jp; shouji@rish.kyoto-u.ac.jp)